RSC Advances

PAPER

View Article Online
View Journal | View Issue

Cite this: *RSC Adv.*, 2026, **16**, 16344

Effect of bleaching process on the allomorph, crystalline index, morphology, and thermal stability of cellulose nanocrystals derived from rice straw

An Nang Vu, *[ab] Ngoc-Uyen T. Nguyen, [ab] Truc-Lam T. Nguyen[c] and Van-Anh T. Nguyen[c]

Rice straw (RS), a renewable byproduct of rice production, represents a promising source of cellulose nanocrystals (CNC). Bleaching is essential for obtaining high-purity cellulose and reducing RS recalcitrance by removing hemicellulose and lignin. This study compares two bleaching methods—alkaline hydrogen peroxide (AHP, Route 1) and hydrogen peroxide-acetic acid (HPAA, Route 2)—and evaluates their effects on the structure and properties of RS-derived cellulose and CNC following H_2SO_4 hydrolysis. Analytical techniques were employed to assess chemical composition, structure, crystallinity, morphology, and thermal properties. Thermogravimetric analysis using the K–K method provided effective measurement of hemicellulose and lignin removal. Route 1 did not fully remove lignin, resulting in CNC1 with a cellulose I structure, high thermal stability, and a rod-like shape. In contrast, HPAA bleaching efficiently removes lignin and introduces carbonyl groups on the cellulose surface, increasing fiber flexibility. This enhances sulfuric acid penetration and disrupts hydrogen-bond networks in both crystalline and disordered regions. H_2SO_4 molecules contribute to dissolution, regeneration, and acid hydrolysis. After H_2SO_4 hydrolysis, CNC2 converts to cellulose II and displays a spherical shape with lower crystallinity and thermal stability than CNC1, mainly due to surface sulfate groups. These results demonstrate that HPAA bleaching is both effective and environmentally preferable for whitening cellulose derived from agricultural waste.

Received 2nd February 2026
Accepted 19th March 2026

DOI: 10.1039/d6ra00911e

rsc.li/rsc-advances

1. Introduction

Cellulose is the most abundant natural renewable resource and serves as a promising alternative to fossil-based materials for achieving low or net-zero carbon emissions.[1,2] It is utilized in writing, printing, packaging, construction, and emerging fields such as healthcare and bioengineering. Cellulose nanocrystals (CNC), derived from cellulose, are under investigation for applications in bioplastics, composites, and electronics, thereby supporting sustainable practices. Cellulose is a high molecular weight homopolymer composed of β-1,4-D-glucose units.[3] It exists in six interconvertible allomorphs—cellulose I, II, III_I, III_{II}, IV_I, and IV_{II}—which differ in hydrogen-bonding networks and chain arrangements.[3,4] Among these, cellulose I and II are the most extensively studied. Cellulose I is present in seeds,[5] wood,[6] straw,[7] bacteria,[8] and certain algae.[9] It features a parallel crystalline arrangement and exists in two phases: Iα, with a triclinic unit cell and one chain per unit,[10] and Iβ, with a monoclinic unit cell.[11,12] In contrast, cellulose II contains antiparallel chains with a monoclinic unit cell aligned along 2-fold screw axes.[13] The conversion of cellulose I to II involves rotation of the hydroxyl groups from the tg to the gt conformation and modification of the hydrogen-bond network.[13,14]

A range of lignocellulosic agroindustrial residues, such as rice husk,[15] wheat straw,[16] banana residues,[17] sugarcane bagasse,[18] orange bagasse,[19] oat hulls, and soybean hulls,[20] serve as promising sources of cellulose. Utilizing these materials alleviates pressure on native forests, preserves biodiversity, maintains biogeochemical cycles, and reduces greenhouse gas emissions by preventing landfill decomposition and methane release. This approach also addresses challenges associated with the disposal of agroindustrial waste.[21,22] Rice straw, a byproduct of rice production, contains 30–36% cellulose, 19–32% hemicellulose, 5–18% lignin,[23–25] and 5.5% silicon.[26] Cellulose and hemicellulose are connected by weak hydrogen bonds, whereas lignin is covalently linked to hemicellulose, forming a robust, insoluble lignin-carbohydrate complex[27] that necessitates harsh processing for biopolymer isolation.[28] Consequently, bleaching is required to break down lignocellulose, remove hemicellulose and lignin, and enhance hydrolyzability.[29]

Traditional lignin-targeting pretreatments, including alkaline, deep eutectic solvent, and organic solvent methods,

[a]Faculty of Materials Science and Technology, University of Science, VNU-HCM, 700000, Vietnam. E-mail: vnan@hcmus.edu.vn
[b]Vietnam National University Ho Chi Minh City, 700000, Vietnam
[c]Ho Chi Minh City University of Industry and Trade, Vietnam

achieve substantial delignification (60–100%) and can dissolve significant amounts of hemicellulose (40–100%). Sodium hydroxide (NaOH) is an effective alkaline agent for removing hemicellulose and lignin by breaking down lignocellulosic structures into fiber components.[30,31] Conventional bleaching frequently employs toxic chlorinated compounds, which are environmentally hazardous. To mitigate these concerns, alternative processes utilizing hydrogen peroxide, such as alkaline hydrogen peroxide (AHP, pH 8–12) and hydrogen peroxide-acetic acid (HPAA), are used to oxidatively degrade residual lignin and hemicellulose and enhance cellulose whiteness.[15,32–34] These methods depend on oxidizers, specifically the hydroperoxide anion (HOO^-) in AHP and peroxyacetic acid in HPAA. Recent research demonstrated that the AHP process effectively removes lignin and hemicelluloses from rice husk (RH), yielding CNC with a diameter of 19 ± 3.3 nm, length of 195 ± 24 nm, and aspect ratio of 10.2 ± 6.8 after hydrolysis with 64% H_2SO_4.[15] The HPAA process operates under mild conditions, without harsh acids, and can remove over 90% of lignin from various materials,[35] achieving effective bleaching even at low concentrations. Additionally, HPAA exhibits strong bactericidal, antimicrobial, and fungicidal properties.[36–40] Although bleaching agents can influence cellulose whiteness and mechanical properties,[35] the effect of HPAA on cellulose derived from RS has not been previously reported. This study examines the extraction and characterization of RS cellulose, focusing on the influence of AHP and HPAA bleaching methods on CNC structure, morphology, and thermal stability, and evaluates the potential of HPAA-extracted cellulose for CNC production.

2. Experiment

2.1. Chemicals and reagents

Rice straw was collected as post-harvest waste in Binh Chanh district, Ho Chi Minh City. The stems were cut into 2–3 cm pieces, rinsed with tap water to remove dust and soluble impurities, and air-dried. The dried straw was ground into a fine powder. Sodium hydroxide (NaOH, 96%), hydrogen peroxide (HP, H_2O_2, 30%), formic acid (FA, HCOOH, 90%), hydrochloric acid (HA, HCl, 37%), acetic acid (AA, CH_3COOH, 99.5%), sulfuric acid (SA, H_2SO_4, 98%), and ethanol (C_2H_5OH, 99.7%) were purchased from Xilong Scientific Co., China, and used as received.

2.2. Isolation of RS cellulose by the AHP process (Route 1)

The AHP process for isolating RS cellulose followed the procedure described in our previous study.[41] Briefly, the RS powder was boiled in distilled water at 100 °C for 2 hours to remove impurities. After filtering and drying, the powder was treated with 90% HCOOH at a 1 : 15 m/V ratio at 80 °C for 2 hours. The resulting material was filtered, rinsed with hot water, and dried at 80 °C for 6 hours. Peroxyformic acid (90% HCOOH, 4% H_2O_2, 6% H_2O) was then added, and the mixture was heated to 80 °C for 2 hours. After filtering, rinsing with distilled water to pH 6–7, and drying at 80 °C for 12 hours, the solid was bleached with an $NaOH/H_2O_2$ mixture. The suspension pH was adjusted to 11 with 1 M NaOH, followed by the gradual addition of 30% H_2O_2 (equivalent to 40% of the solid mass). The mixture was stirred for 1 hour at 80 °C.

2.3. Isolation of RS cellulose by the peracetic acid (HPAA) process (Route 2)

The ground RS material (10 g) was washed separately in 200 mL of 0.1 M HCl for 2 hours at 100 °C under mechanical stirring. Then, the material was recovered by Buchner filtration, washed with 20 mL of fresh water, and air-dried overnight. 10 grams of RS treated with HCl were then treated with 200 mL of 0.1 M NaOH for 2 hours at 100 °C under mechanical stirring. The cellulose-rich insoluble material was separated by filtration and washed with 20 mL of 0.1 M NaOH solution. The product was then air-dried. After treatment with HCl and NaOH, 20 g of fibers were placed in a flask, and 250 mL of a peracetic acid solution (50% CH_3COOH, 38% H_2O_2, 1.5% H_2SO_4, and 10.5% H_2O) was added. The recirculation system was installed, and the mixture was stirred mechanically at 95 °C for 4 hours. Then, the fibers were vacuum-filtered, washed with clean water until the pH was about 6–7, and air-dried.

2.4. Production of cellulose nanocrystals (CNC)

RS cellulose was broken down using a 64% SA solution (1 : 20 solid mass to acid volume ratio) at 45 °C for 30 minutes to produce CNC. The mixture was carefully transferred to a container with 1000 mL of distilled water to complete the process. The solution was diluted with water until the pH reached 7. The mixture was centrifuged at 6000 rpm for 10 minutes, twice with distilled water and three times with ethanol. A sample of white powder was obtained after drying at 80 °C until a constant weight was reached.

2.5. Characterizations

2.5.1. Fourier transform infrared (FT-IR) spectroscopy. FT-IR spectroscopy (PerkinElmer, USA) was used to analyze the chemical structure of RS and CNC. Oven-dried samples (2 mg) were combined with 200 mg of potassium bromide (KBr) and pressed into transparent pellets. Spectra were collected in transmittance mode at a 2 cm^{-1} resolution, spanning 4000 to 400 cm^{-1}, and averaged over 32 scans.

2.5.2. X-ray diffraction (XRD) analysis. X-ray diffraction (XRD) was used to analyze structural changes in the treated materials at each stage. Crystallization characteristics were measured with a Bruker D2 Phaser diffractometer using Cu Kα ($\lambda = 0.15406$ nm), operating at 30 kV and 10 mA. Samples were mounted on a quartz substrate, and data were collected at a scanning rate of 0.02° min^{-1} over a 2θ range of 10–80°. Each sample underwent two XRD analyses. Diffraction peaks were refined and analyzed with Xpert Highscore Plus software (PANalytical Technologies Pvt. Ltd, Netherlands). The curves were fitted using a Gaussian function in OriginPro 9.0.0 (64 bit) (OriginLab Corporation, United States). The crystallinity index (CrI) was calculated from the areas under the crystalline and

amorphous peaks after baseline correction, using eqn (1) below.[42]

$$\mathrm{CrI}\ (\%) = A_c/(A_c + A_a) \times 100 \quad (1)$$

where A_a denotes the area under the amorphous peaks, and A_c is the area of the crystalline peaks.

2.5.3. Transmission electron microscopy (TEM) analysis. CNC morphology was examined using TEM (JOEL, JEM-2100, Japan) at 200 kV. The suspension was diluted in deionized water to 0.04 wt% and sonicated for 10 minutes. The resulting suspension was deposited onto a copper mesh grid for measurement. The collected data were analyzed using ImageJ software.[43] Approximately 100 particles were randomly selected for statistical analysis of their length and width.

2.5.4. Thermogravimetric (TGA) analysis. Thermogravimetric analysis using a TA Instruments TGA Q500 was performed to evaluate the thermal breakdown of materials after each treatment. Samples of 15–20 mg were heated from ambient temperature to 800 °C at 10 °C min^{-1} in nitrogen.

2.5.5. Raman spectroscopy analysis. Raman spectra were collected using laser Raman microspectroscopy (XploRA Plus, Horiba) with a 785 nm excitation wavelength and 0.5 mW power to minimize laser heating effects on the cellulose materials. Each spectrum represents the average of three scans from different CNC sample areas. All spectral modifications were performed using Origin Pro 9.0.0 (OriginLab Corporation, United States).

2.5.6. Solid-state ^{13}C nuclear magnetic resonance (ss-^{13}C NMR). Solid-state ^{13}C NMR measurements were performed on a Bruker AVANCE 400 spectrometer using cross-polarization with high-power proton decoupling and magic-angle spinning (CP/MAS). Spectra were collected at 298 K with a 4 mm probe set to 100.13 MHz. The MAS rotation speed was 12 kHz, the CP contact time was 2 ms, and the repetition interval was 1 s.

2.5.7. Zeta potential. The zeta potential of CNC was determined using Nanopartica sz-100 (Horiba Scientific, Japan). Aqueous suspensions of 0.1 wt% CNC were prepared, and the measurements were performed at 25 °C with a scattering angle of 90°.

3. Results and discussion

3.1. Physical appearance of RS at different treatment stages

Rice straw (RS) consists primarily of cellulose, hemicellulose, lignin, and wax. Cellulose is alkali-resistant, rigid, and rapidly hydrolyzed by acids. Hemicellulose dissolves in alkaline solutions and is degraded by acids. Lignin is soluble in hot alkali, does not hydrolyze in acids, but readily oxidizes and forms aggregates with phenol.

Fig. 1 shows that RS changes color from light brown to reddish brown after FA and PFA treatment (Route 1), then becomes clear white after bleaching, reflecting the removal of hemicellulose, lignin, and other non-cellulosic substances. FA treatment partially dissolves hemicellulose, wax, and pectin. Remaining lignin swells in the FA solution and migrates to the surface, facilitating the PFA process. At this stage, the sample appears a deeper reddish-brown due to phenol derivatives in lignin absorbing visible light. The PFA step softens the fiber by removing large amounts of hemicellulose and some lignin with H_2O_2 as the oxidant. Unlike FA treatment, lignin remains on the fiber surface, swells, and moves outward, resulting in a darker color after PFA treatment. Although FA and PFA treatments effectively extract most hemicellulose, wax, and pectin from RS, further bleaching is required to remove lignin and obtain purified cellulose.

The process of lignin degradation by H_2O_2 has been proposed and studied, demonstrating that the free radicals produced by H_2O_2 in alkaline solutions are primarily responsible for the disintegration of the lignin structure. In an alkaline solution (with an optimal pH of 11.5), a large amount of hydroperoxy radicals (HO_2^-) is produced, which then leads to the formation of more hydroxyl radicals ($^{\bullet}OH$). The hydroperoxy radical acts as a nucleophilic reagent, primarily to catalyze a redox reaction with lignin's chromophores to improve the slurry's brightness. The hydroxyl radical, an electrophilic reagent with a very high redox potential, can break down the lignin structure. This process enhances the slurry's whiteness and improves purification.[44]

In Route 2, after HCl treatment, RS forms a fine powder with a darker color than the original sample (Fig. 1). Following NaOH treatment, the sample turns yellow-brown. HCl and NaOH treatments dissolve and remove amorphous hemicellulose and lignin from the surface, exposing the underlying cellulose. NaOH at 100 °C reacts with –OH groups on the polysaccharide surface, forming alkoxide groups and reducing intra- and intermolecular hydrogen bonds in RS. NaOH also dissolves non-cellulose components such as hemicellulose, pectin, and wax, and partially breaks down lignin.

HPAA pretreatment was then applied to remove lignin from RS. Previous studies[45] show that HPAA effectively delignifies lignocellulosic materials, removing over 90% of lignin. Ying *et al.*[44] reported that using 100 mM H_2SO_4 as a catalyst in HPAA pretreatment achieves 86.1% lignin removal from poplar while preserving high levels of glucan (>94%) and xylan (>84%). Lignin is the main colored component in RS. After HPAA treatment, RS becomes pure white, indicating highly efficient lignin extraction.

HPAA consists of hydrogen peroxide, acetic acid, and peracetic acid. In this study, HPAA was produced by reacting hydrogen peroxide with acetic acid in the presence of SA, a strong mineral acid.[46] Acetic acid reacts with hydrogen peroxide in an acidic environment to generate the highly oxidizing peracetic acid, which then releases oxygen radicals that attack the β-aryl ether bonds in lignin and the glycosidic bonds in carbohydrates (cellulose and hemicellulose), ultimately breaking them down into water-soluble small molecules acid.[46]

Cellulose fiber is a semi-crystalline material with both crystalline and amorphous regions. Acid hydrolysis primarily targets amorphous regions, as acids release hydronium ions (H^+) that break glycosidic and ether bonds in these regions. After acid hydrolysis, CNC colloidal suspensions were uniform and stable.

Fig. 1 RS photographs at different treatment stages.

3.2. Fourier transform infrared (FT-IR) spectroscopy

Fig. 2 displays the FT-IR spectra of RS after various treatments *via* Route 1 and CNC1 prepared by acid hydrolysis. The absorption peaks in all spectra at 3420, 2908, 1380, and 898 cm^{-1} are characteristic of cellulose structure.[47–50] The FT-IR spectrum of untreated RS shows a broad peak at 3420 cm^{-1}, which results from the O–H group stretching vibrations of hydrogen-bonded hydroxyl groups found in cellulose, hemicellulose, and lignin.[51] Small absorption bands at 3850 cm^{-1} and 3740 cm^{-1} originate from the vibration of free O–H groups, which can be present in pectin, waxes, and other impurities.[52] The spectrum also features a peak at 1740 cm^{-1}, attributable either to the acetyl and uronic ester groups of hemicelluloses or to the ester linkage of carboxylic groups in ferulic or *p*-coumaric acids of lignin and hemicelluloses. The peak at 1515 cm^{-1} represents the aromatic C=C stretch of lignin's aromatic rings, while the peak at 805 cm^{-1} indicates the vibration of mannan in hemicellulose and the out-of-plane bending of CH in phenyl rings.

The absence of these peaks in AHP-treated fibers is due to lignin removal during the treatment. The lack of bands at 3850, 3740, 1465, 1425, and 1265 cm^{-1} indicates the successful removal of lignin, hemicelluloses, and other contaminants in the AHP-treated fibers.[53] The FT-IR spectrum of AHP-treated RS also shows characteristic absorption bands at 1160, 1100, 1055, and 1025 cm^{-1} that relate to the structure of cellulose. The peaks at 1160 and 1100 cm^{-1} result from the asymmetric and symmetric stretching of the –C–O–C– bond in cellulose. The peaks at 1055 and 1025 cm^{-1} correspond to the C–O stretching of secondary and primary alcohol groups in cellulose. The small, sharp band at 898 cm^{-1} shows the β-glucosidic bond in the cellulose molecule.[54] After AHP treatment, this band becomes more intense, indicating a higher degree of cellulose purity. This suggests that, following chemical treatment, hemicellulose and lignin are effectively removed, exposing the cellulose.[52]

The FT-IR spectrum of CNC1 shows no new absorption peaks compared to the FT-IR spectrum of AHP-treated RS, indicating that the cellulose structure remained unchanged after hydrolysis with H_2SO_4. The absorbance peak at 710 cm^{-1} signifies a monoclinic cellulose structure (Iβ), which is known to be a highly thermodynamically stable allomorph.[55]

Fig. 3 presents the FT-IR spectra of RS after various treatments using Route 2 and of CNC2 prepared *via* H_2SO_4

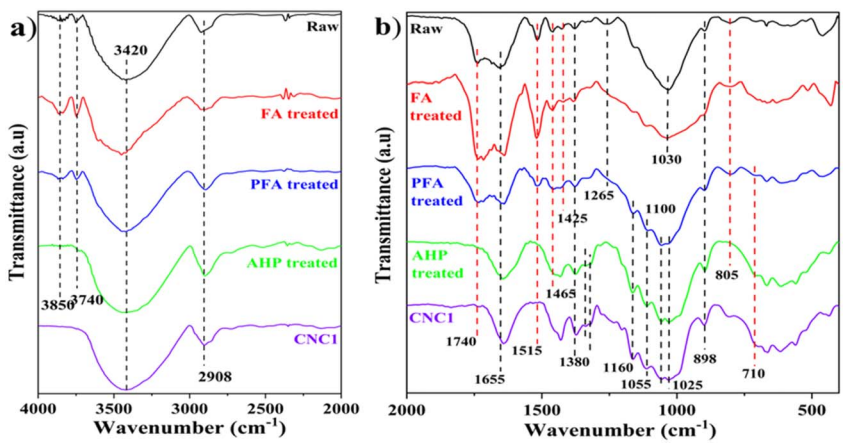

Fig. 2 FT-IR spectra of RS after different treatments *via* Route 1 in the range of (a) 4000–2000 cm^{-1} and (b) 2000–400 cm^{-1}.

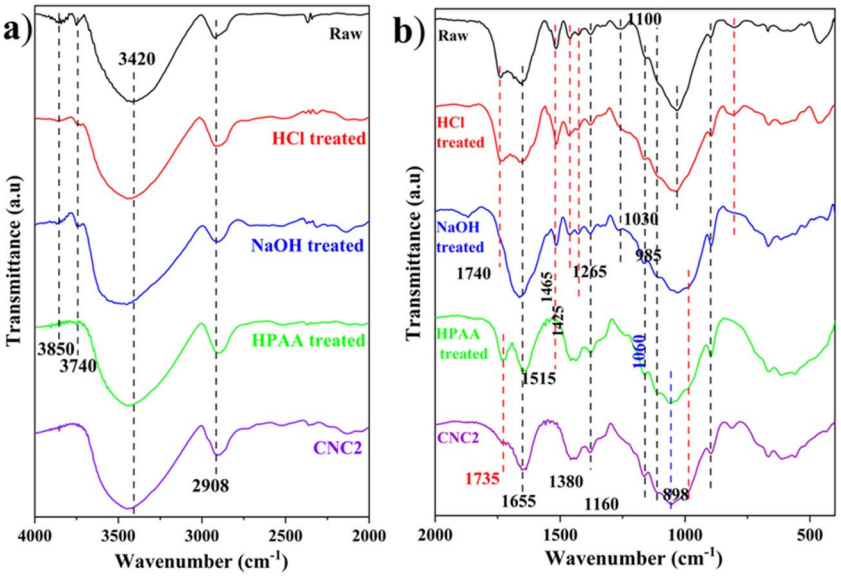

Fig. 3 FT-IR spectra of RS after different treatments *via* Route 2 in the range of (a) 4000–2000 cm^{-1} and (b) 2000–400 cm^{-1}.

hydrolysis. Similar to Route 1, the chemical treatment removed lignin, hemicelluloses, and other impurities from RS. After NaOH treatment, the absorption band at 1740 cm^{-1}, which corresponds to the stretching vibrations of acetyl C–O and ester C═O in hemicelluloses and lignin, nearly disappeared. However, the FT-IR spectrum of RS treated with HPAA showed a peak at 1735 cm^{-1}, indicating the formation of carboxyl groups during the oxidation of cellulose hydroxyl groups under the effect of peracetic acid.[56,57] It has been reported that the degree of oxidation (DO) can be calculated by the ratio of the carbonyl peak's intensity to that of the strongest band near 1060 cm^{-1}, which is related to the backbone structure of cellulose. The relationship derived from previously published results, $DO = 0.01 + 0.7\ (I_{1735}/I_{1060})$, could be applied here.[58] The calculated DO values are 0.354 and 0.193 for the HPAA-treated and CNC2 samples, respectively. Therefore, the degree of oxidation of CNC2 is lower than that of HPAA-treated RS. Both FT-IR spectra of HPAA-treated RS and CNC2 show a small peak at 985 cm^{-1}, which corresponds to the C–O stretching vibration of cellulose. The small shoulder at 811 cm^{-1}, visible only in CNC2, indicates the vibration of the C–O–SO_3 group. This phenomenon results from sulfonate esters present on the cellulose surface during H_2SO_4 acid hydrolysis.[59,60] Additionally, the FT-IR spectra of both samples do not show absorption peaks at 710 cm^{-1} and 750–760 cm^{-1}, which are characteristic of the Iβ (monoclinic) and Iα (triclinic) allomorphs, respectively.[61]

3.3. X-ray diffraction analysis (XRD)

Fig. 4 shows the X-ray diffraction (XRD) analysis of untreated and chemically treated RS when applying Route 1 (Fig. 4a) and Route 2 (Fig. 4b). The XRD spectra reveal three prominent peaks at 15.5°, 21.5°, and 35.0° in all samples before hydrolysis with H_2SO_4, which are identified as cellulose polymorph I, maintained at each stage of isolation.[55]

The peak at 21.5° indicates the distance between 2D planes in the 3D stack, held together by van der Waals forces. Intermolecular and intramolecular hydrogen bonds connect the cellulose molecules that make up each 2D plane. This complex network of hydrogen bonds and van der Waals interactions arranges the cellulose chains into semi-crystalline polymers. Even in untreated RS, although only a broad crystalline signal is visible, the cellulose I crystalline structure can still be observed.[44]

After hydrolysis with H_2SO_4, cellulose treated with AHP preserves the polymorphic structure of cellulose I. Meanwhile, the presence of four well-resolved peaks at 2θ = 12.1°, 19.8°, 21.7°, and 34.5° in the diffractogram of CNC2, obtained by hydrolyzing the cellulose according to Route 2 (Fig. 4b), indicates the dominance of cellulose with structure II.[62]

According to our previous study,[63] the peak deconvolution technique was used to isolate specific crystalline peaks from XRD curves to determine the crystallinity of materials produced at various stages (Fig. S1). All peaks were fitted with Gaussian functions, and the broad peaks around 20° and 40° were attributed to the amorphous contribution. In cellulose, an amorphous peak is frequently observed in the 2θ range of 16–20°.[64–66]

This study associated a broad peak around 35° with the crystallinity component, aligning with the experimental data. According to Fig. 5, the RS treated with the AHP process shows an increased CrI. The crystallinity of the extracted cellulose was notably higher than that of the raw straw material, indicating that FA, PFA, and AHP treatments removed lignin, hemicellulose, and pectin, thereby enhancing crystallinity.[67] After acid hydrolysis, a prominent peak emerged in the XRD pattern, indicating a significant increase in crystallinity. Hydronium ions (H_3O^+) penetrated amorphous regions and facilitated the hydrolysis of cellulose's glycosidic bonds, thereby releasing individual crystallites.[65,68–70]

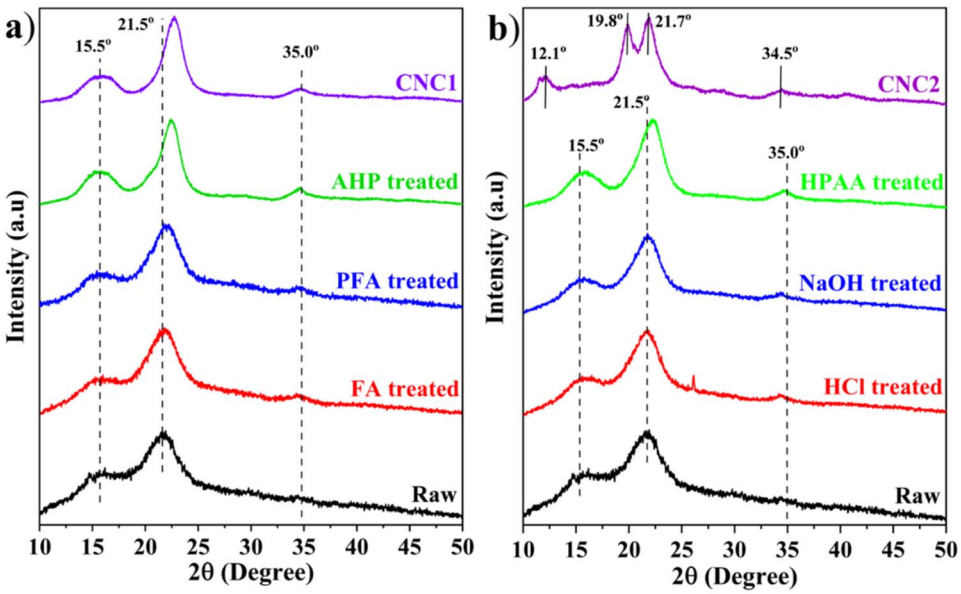

Fig. 4 XRD patterns of untreated and treated RS for (a) Route 1 and (b) Route 2.

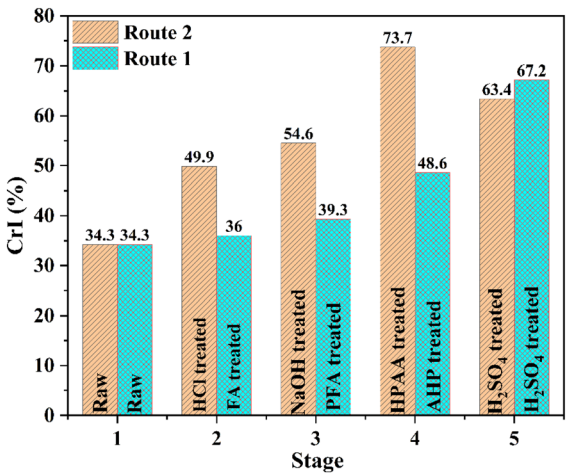

Fig. 5 The CrI chart of RS at different treatment stages.

When treated according to Route 2, the CrI value of RS also increased from the raw sample through the treatment steps, including HCl-treated, NaOH-treated, and HPAA-treated. Compared to Route 1, the removal of amorphous components such as lignin, hemicellulose, and pectin from RS when treated with HCl, NaOH, and HPAA on Route 2 was more effective. The CrI value of RS was 73.7% after treatment with HPAA solution, compared to 48.6% after treatment with AHP solution in Route 1. HPAA removed more non-cellulosic components while increasing the amount of crystalline cellulose,[71,72] because the oxygen radicals generated by the HPAA reaction attack the β-aryl ether bonds in lignin, causing lignin to break into smaller fragments and undergo a series of reactions leading to its eventual conversion into small water-soluble molecules.[73,74] Hemicellulose and the amorphous regions of cellulose are, on the other hand, oxidatively destroyed at high temperatures under the intense oxidizing environment created by HPAA.[73] This process will be discussed in detail in Section 3.4.

The crystallinity of HPAA-treated RS exceeded that of corncob (52.8%)[75] and oil palm fronds (62.3%),[76] both of which were treated with acidified sodium chlorite and different levels of HCl. Additionally, the crystallinity of cellulose from pomelo peel (40.5%),[77] rose stems (70.2%),[78] and soybean hulls (70.0%)[79] was lower than that of HPAA-treated RS. The crystallinity of HPAA-treated RS was also similar to brown algae (74.2%)[71] and olive fiber (74.2%),[80] but lower than roselle fibers (78%)[81] and black tea waste (89.8%).[82] Although cellulose has been successfully extracted from various biomasses using these methods, the drawbacks are clear: high toxicity of halogenated reagents to humans and the environment, lengthy processing times, high reagent consumption, equipment corrosion from strong acids, and increased reprocessing costs. In comparison, HPAA is an affordable and eco-friendly method for extracting cellulose.[83]

However, after hydrolysis with H_2SO_4, the CrI value decreased. The reduction of CrI in CNC2 may be caused by a polymorphic transformation.[84] As mentioned earlier, peracetic acid during HPAA treatment oxidizes hydroxyl groups in cellulose, producing carboxyl groups. The formation of carbonyl groups on the surface of cellulose nanoparticles would make these particles more reactive and increase their flexibility.[85] When low temperatures (45 °C) and high SA concentrations (64%) are used, cellulose can become completely soluble within the first few minutes. A concentrated aqueous SA solution could simultaneously disrupt hydrogen-bond networks in both crystalline and disordered regions. It was highly likely that the crystalline cellulose dissolved in concentrated SA still retained some degree of order. Specifically, the arrangement of cellulose chains was not entirely random but resembled a highly swollen state. With a short reaction time, the cellulose intermediate

recrystallizes into cellulose II, which is more thermodynamically stable;[62] the original parallel chains of cellulose I change to anti-parallel in cellulose II. Dissolution and subsequent regeneration result in a structural transition from cellulose I to cellulose II, accompanied by a decrease in crystallinity.[86]

Another potential reason for decreased crystallinity is partial damage to cellulose's crystalline regions. The introduction of negative carboxyl groups loosens the compact structure of cellulose by disrupting intra- and intermolecular hydrogen bonds, thereby enhancing the diffusion of H_2SO_4 molecules and increasing the hydrolysis rate.[87] Consequently, both amorphous and crystalline regions of cellulose are hydrolyzed. The processes of dissolution, regeneration, and acid hydrolysis can occur simultaneously upon introduction of H_2SO_4.

3.4. Thermogravimetric analysis

TGA is used to predict the thermal performance of RS at various processing stages by measuring the rate of weight change with temperature (°C) under a nitrogen atmosphere. Changes in thermal stability caused by chemical treatments (such as FA, PFA, AHP, and SA) on the raw fibers can be evaluated through TGA and the first derivative of thermogravimetric analysis (DTG) curves (Fig. 6a). Fig. 6b shows that the pyrolysis process of RS at 10 °C min^{-1} can be divided into three stages: drying below 200.0 °C, devolatilization between 200.0 and 500.0 °C, and the degradation of char and minerals above 500.0 °C.

The weight loss of RS was caused by water evaporation at low temperatures during the first stage and occurred within the 200.0–500.0 °C range during the main devolatilization stage. The total weight loss of 60.49% in this main stage was linked to increased volatilization from the breakdown of organic compounds, including (hemi-)celluloses, partial lignin, and other macromolecules, as well as a lower fixed carbon content in the sample.

To estimate the peaks of hemicellulose, cellulose, and lignin during pyrolysis, the absolute value of the second-order derivative (|DDTG|) was calculated from the TG curves.[88] For each of the three components, the temperature where the absolute value of DDTG reaches a local minimum was considered the peak temperature (Fig. 6c). After identifying the peak temperature, the DTG curves were deconvoluted using an asymmetric bi-Gaussian function in Origin 2025 software (Fig. 6d). This method, known as the K–K method, was developed by Li *et al.*[89] and has been used to analyze the thermal degradation of wastewater sludge, waste tea bamboo residue, and rice husk. In

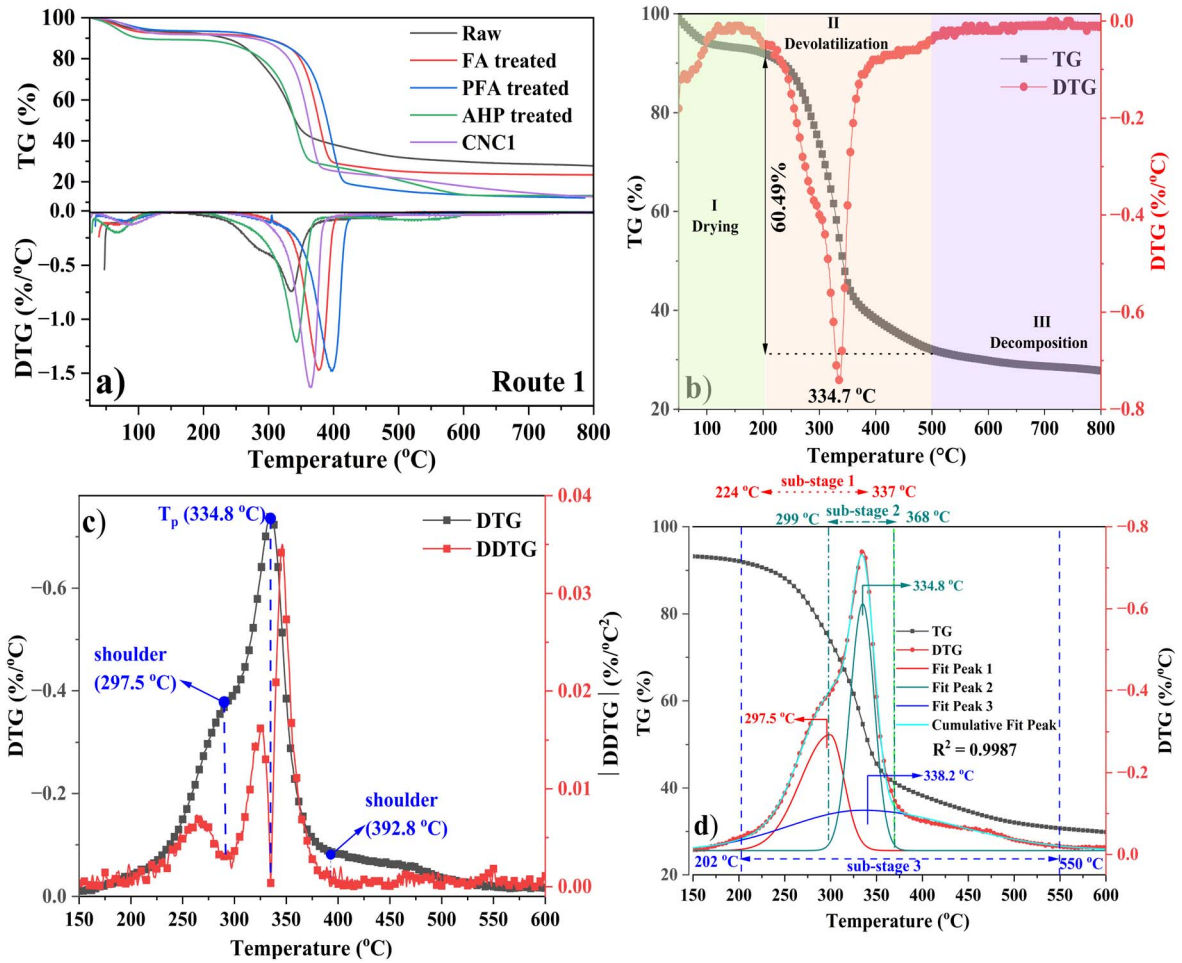

Fig. 6 TGA and DTG curves of (a) RS pyrolysis, (b) stage division, (c) sub-peak detection, and (d) devolatilization stage deconvolution.

this study, we applied this method not only to raw RS but also to RS at different chemical treatment steps to evaluate the removal of hemicellulose and lignin from RS.[90]

Fig. 6d shows the deconvolution of the RS devolatilization phase divided into three sub-stages.[91] The curve's high goodness-of-fit (0.9987) indicates that the asymmetric bi-Gaussian function model accurately describes the deconvolution process (Fig. 6d). In the first sub-stage (pseudo-hemicellulose), weight loss was mainly due to hemicellulose degradation, with its primary decomposition temperature ranging from 224.0 to 337.0 °C (Fig. 6d). In the second sub-stage (299.0–368.0 °C), weight loss was primarily caused by the thermal breakdown of cellulose and smaller amounts of lignin (pseudo-cellulose). Cellulose is a high-molecular-weight compound with a long linear chain made of D-glucosyl groups and has a crystalline structure composed of ordered microfibrils, making its thermal degradation more difficult than that of hemicellulose. The weight loss observed during the third sub-stage (202.0–550.0 °C) mostly results from the decomposition of lignin (pseudo-lignin). Yang *et al.*[92] noted that, regarding thermal degradation, the three main biomass components, listed from easiest to hardest to decompose, are hemicellulose, cellulose, and lignin. Tsamba *et al.*[93] observed that lignin starts to decompose at low temperatures (160–170 °C) and continues at a slow rate until about 900 °C. Hemicellulose is the second component to decompose, followed by cellulose, within a narrow temperature range of roughly 200 to 400 °C. Accordingly, the three sub-stages likely correspond to hemicellulose, cellulose, and lignin, respectively. The RS residues were estimated at 27.80% after pyrolysis in the N_2 atmosphere.

Fig. 7 shows the width of the deconvoluted DTG devolatilization peaks of RS after various chemical treatment steps. When RS is processed with Route 1, only two deconvoluted DTG peaks are observed within the temperature range of 150–600 °C (Fig. S2). These peaks represent pseudo-hemicellulose (sub-stage 1) and pseudo-cellulose (sub-stage 2). When RS is soaked in an FA solution at 80 °C (FA-treated), hemicellulose partially dissolves, causing lignin to swell and migrate to the surface. The lignin on the surface raises the initial decomposition temperature for sub-stage 1 in FA-treated RS (264 °C instead of 224 °C for untreated RS). Additionally, the temperature range for this stage in FA-treated RS (264–475 °C) is wider than in untreated RS (224–337 °C) due to the decomposition of residual hemicellulose and lignin on the surface.

The PFA and AHP treatment stages were further carried out to remove hemicellulose and lignin. The removal of these two amorphous components was indicated by a narrowing of the decomposition temperature range in sub-stage 1 (Fig. 7) and an increase in the CrI value (Fig. 5). However, the results in Fig. 7 also show that, after AHP treatment, the amount of lignin remaining in the original RS was not eliminated. This phenomenon was not observed in the FT-IR spectrum but will be examined and discussed in the Raman spectrum analysis in Section 3.5. Finally, hydrolysis with SA completely removed lignin, resulting in pure cellulose. The DTG diagram of CNC1 also displays two substages. Sub-stage 1 reaches a maximum decomposition temperature of 355.9 °C, corresponding to the decomposition of amorphous cellulose, while sub-stage 2, related to crystalline cellulose decomposition, has a maximum temperature of 368.3 °C.

The thermal stability trend of RS after removing hemicellulose and lignin with Route 2 was similar to that of Route 1. However, DTG analysis indicated that the HPAA treatment stage produced materials with higher thermal stability than those processed with AHP and CNC1. The DTG curve for HPAA-treated RS also shows two phases. The first stage had a maximum decomposition temperature of 369.2 °C, indicating the breakdown of –COOH side-chain functional groups. The second stage reached 407.7 °C, indicating that the cellulose main chain

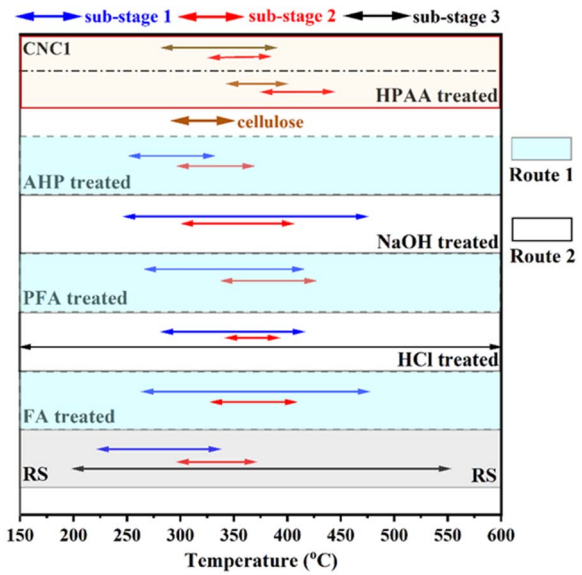

Fig. 7 The width of the deconvolution peaks of the devolatilization stage of untreated and treated RS.

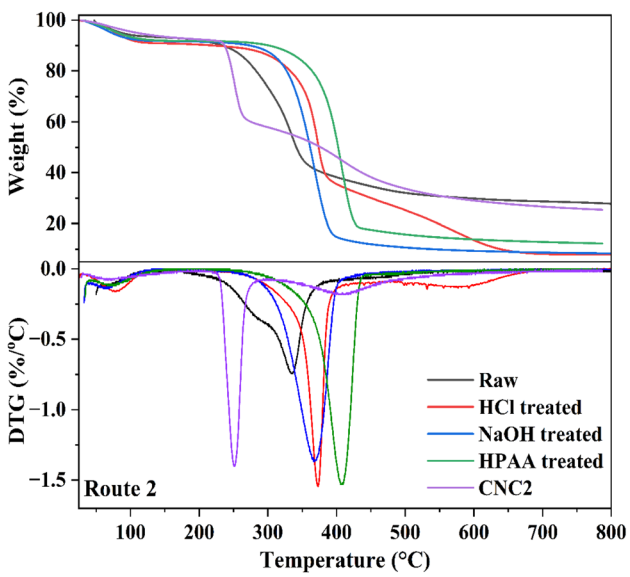

Fig. 8 TG and DTG curves of RS pyrolysis when processed through Route 2.

broke down. In contrast to HPAA-treated RS, CNC2 showed a notable difference in decomposition behavior (Fig. 8).

CNC2 exhibited a two-step degradation that was less extensive than that of HPAA-treated RS. The lower thermal stability can be attributed to two reasons: (1) the microsphere shape of CNC2 (discussed in Section 3.6) increases the surface area exposed to heat, (2) the presence of more sulfate groups on the surface may lower the degradation onset temperature.[94] The results are correlated with the presence of sulfate ester groups, as shown in the Raman spectrum below (Fig. 9). The next stage occurred between 290 °C and 580 °C and was attributed to oxidation and breakdown of charred residues, releasing low-molecular-weight gaseous products.[95,96] The carbon residues formed by CNC2 were higher than those in CNC1. This increase was due to the increased content of sulfate groups and their counterions. The traditional view suggests that cellulose II is more thermally stable than cellulose I, but this assumption is based on pure cellulose. Therefore, the observed reduction in thermal stability in CNC-II does not conflict with this idea, as it results from changes in its specific surface area and from increased sulfate groups during nanonization.

3.5. Raman spectroscopy analysis

AHP-treated RS, CNC1 (Route 1) and HPAA-treated RS, CNC2 (Route 2) were examined in their characteristic vibrational modes using Raman spectroscopy with a 785 nm excitation source, as shown in Fig. 9. Here, we focused on vibrational modes in the conformationally sensitive range below 1600 cm^{-1}, which is preferred for characterizing polymorphic changes. All the major Raman bands observed in the spectra are listed in Table S1 of the SI, with vibrational modes assigned according to the literature.[97–100] However, it should be noted that most of the cellulose vibrational modes are highly coupled,[101] and therefore, the assignments are approximate.

As shown in Fig. 9a, the AHP treatment induces the formation of cellulose II, resulting in several new spectral features, indicated by a cross for clarity. Mercerization, or regeneration of native cellulose, changes cellulose I into cellulose II. NaOH molecules can penetrate the crystalline regions of cellulose, break hydrogen bonds, and cause swelling or dissolution of crystalline cellulose. The dissolved cellulose then recrystallizes to form cellulose II particles. The Raman band around 820 cm^{-1} also indicates the impact of alkaline treatment on the supramolecular structure of cellulose.[97,99,102] Amorphous cellulose is characterized by a prominent absorption peak at 1092 cm^{-1}.[97] Additionally, the Raman spectrum of AHP-treated RS shows a band near 1600 cm^{-1}, corresponding to the ν(C=C) aromatic stretching mode, which is typical of lignin.[103,104] This finding aligns with the TGA analysis results discussed earlier. Therefore, structurally, AHP-treated RS exhibits a combination of the crystalline structures of cellulose I and II.

In the CNC1 spectrum, a band at 595 cm^{-1} appears, characteristic of δ(CCH) twisting in cellulose type I. Additionally, relatively strong bands at 332 cm^{-1}, due to δ ring twisting, and at 971 cm^{-1}, resulting from ν(C–C), ν(C–O), or $\rho(CH_2)$ vibrations in cellulose I, are observed. Another confirmation of cellulose I content is the absence of bands at 308 cm^{-1}, 896 cm^{-1}, 1265 cm^{-1}, 1374 cm^{-1}, and 1413 cm^{-1}. Furthermore, the Raman spectra from CNC1 show that the band at 1600 cm^{-1} is completely absent, and the band at 1092 cm^{-1}, which can be attributed to amorphous cellulose, is significantly reduced.

During the H_2SO_4 hydrolysis process, the H_2SO_4 molecules completely removed the remaining lignin, disrupted the amorphous region, and preserved the cellulose I crystal region. This caused the CrI value of RS to increase sharply as it transitioned from the AHP stage to hydrolysis with H_2SO_4. The removal of lignin and amorphous cellulose primarily accounts for the significantly higher crystallinity of CNC1 compared to AHP-treated RS (Fig. 5).

Fig. 9b shows the Raman spectra of HPAA-treated RS and CNC2. The band at 1600 cm^{-1}, typical of lignin, is completely missing from the spectra of HPAA-treated RS. This indicates that HPAA treatment fully removed lignin from RS. This

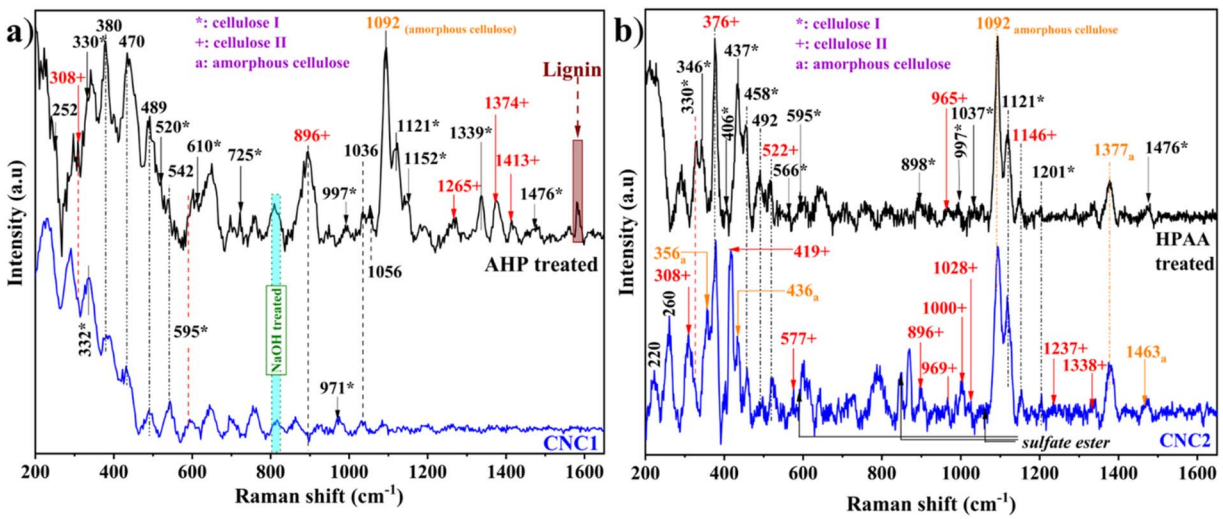

Fig. 9 Raman spectra of (a) AHP-treated RS and CNC1 (Route 1), and (b) HPAA-treated RS, CNC2 (Route 2) in the range of 200–1600 cm^{-1}.

matches the DTG analysis results using the K–K method in Fig. 7. In the spectrum of HPAA-treated RS, three bands appear at 376 cm^{-1}, 522 cm^{-1}, and 1146 cm^{-1}, which are characteristic of the δ(CCC) ring, the ν(CCO) glycosidic ring, and the δ(HCO) bending in type II cellulose, respectively. The faint band at 965 cm^{-1} supports the presence of cellulose II, caused by ν(C–C) and ν(C–O) or $\rho(CH_2)$ vibrations in cellulose II. Other bands represent the cellulose I crystal lattice.

Raman spectroscopy shows that the CNC2 sample has a cellulose II structure after hydrolysis. The bands at 419 cm^{-1} (bending δ(CCO) and δ(CCC)), 896 cm^{-1} (ν(COC) in-plane symmetric), 1000 cm^{-1} ($\rho(CH_2)$), and 1237 cm^{-1} (δ(COH) out of plane) are typical for the cellulose II lattice. The Raman spectrum at 577 cm^{-1}, δ(C–C–H) twisting, is assigned to in-plane heavy stretching, scissoring, and twisting of carbon atoms, indicating cellulose II.[97] This band is unique because it is absent from the Raman spectra of cellulose I and amorphous cellulose. Comparing the spectra of HPAA-treated RS and CNC2, we see new bands in CNC2 that come from sulfate groups. These bands are found at 589 cm^{-1}, between 825 and 845 cm^{-1}, and between 1065 and 1075 cm^{-1}. The band at 589 cm^{-1} is likely due to δ(O═S═O) deformation vibration. The band between 825 and 845 cm^{-1} relates to the ν(C–O–S) stretch vibration. The band from 1065 to 1075 cm^{-1} is linked to the ν_s(O═S═O) symmetric stretch vibration.[105,106] These findings are consistent with the identification of element S in the CNC2 EDX spectrum (Fig. S3).

Thus, the Raman spectra perfectly match the XRD and TGA results mentioned above. After the HPAA treatment, carbonyl groups form on the cellulose surface, increasing the particles' reactivity. This allows easier penetration of sulfuric acid and disrupts hydrogen-bond networks in both crystalline and disordered regions. H_2SO_4 molecules participate simultaneously in dissolution, regeneration, and acid hydrolysis processes. Most of the cellulose loses its crystallinity and transforms into cellulose II during regeneration.[86,107] The lower thermal resistance of CNC2 results from sulfate groups present on its surface during H_2SO_4 acid hydrolysis.

3.6. TEM

Fig. 10 shows the morphology of CNC1 and CNC2. As shown in Fig. 10, two distinct morphologies of CNC are visible in the TEM images: rod-like particles for CNC1 and nearly spherical particles for CNC2. This shape difference can be explained by the role of H_2SO_4 in the hydrolysis process. For Route 1, H_2SO_4 molecules fully remove lignin from the surface of AHP-treated RS, then diffuse and attack the amorphous cellulose, breaking chains into small, soluble oligosaccharides and sugars, resulting in crystalline CNC1. During self-assembly, these CNC1 particles align well and form more organized, possibly crystalline interfaces that exceed the crystalline order in the AHP-treated RS. This improved organization and alignment during CNC1 assembly suggest more uniform particle sizes and/or more highly ordered surfaces, allowing close packing and hydrogen bonding between CNC1 particles. This process leads to the formation of larger, more crystalline bundles, which eventually develop into fibers. It is expected that producing CNC1 through acid hydrolysis and self-assembling it into fibril structures will preserve the same crystalline structure of cellulose I.

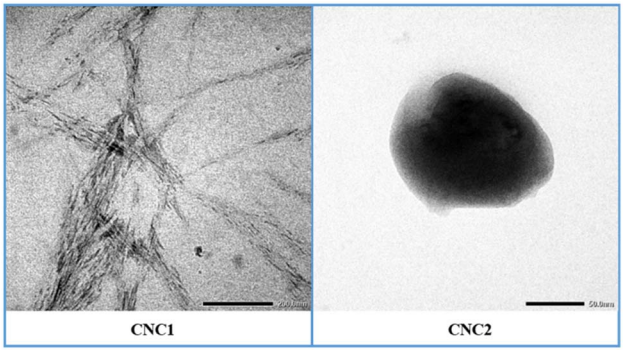

Fig. 10 TEM images of CNC1 (scale bar: 200 nm) and CNC2 (scale bar: 50 nm).

In contrast, for Route 2, cellulose HPAA-treated RS undergoes two main interactions in SA. The first is hydrolysis, which involves breaking the β-1,4-glycosidic bonds. The second involves swelling, dissolving, and the subsequent regeneration of cellulose chains. During hydrolysis, hydrogen ions from the acid attack and break down the loose, amorphous regions of cellulose while leaving the crystalline areas intact. As a result, native microfibrils transform into short rods and then into smaller nanoparticles with irregular shapes.[108] SA also causes surface esterification, producing acid half-esters or cellulose sulfate on the CNC2 surfaces, which results in negatively charged surfaces that repel each other during regeneration. Celluloses with lower surface charges remain buried within and are connected *via* hydrogen bonds or hydrophobic interactions, forming cellulose microspheres.[109,110] Another reason for the formation of cellulose microspheres is that cellulose tends to assemble into a thermodynamically stable spherical shape.[111–113]

ImageJ analysis showed that CNC1 has an average length of 514 ± 90 nm and a diameter of 38 ± 6 nm. CNC2 displays a spherical shape with an average diameter of 117 ± 20 nm. The colloidal stability of CNC1 and CNC2 was evaluated using zeta potential measurements. As shown in Fig. S4, CNC1 had an average zeta potential of −28.4 mV, indicating a tendency to agglomerate and settle. In comparison, CNC2 exhibited a significantly higher average zeta potential of −42.6 mV, demonstrating greater colloidal stability. The introduction of sulfate groups to CNC2 during H_2SO_4 hydrolysis improved its dispersion in water through electrostatic repulsion.

3.7. ^{13}C-NMR analysis

Fig. 11 displays the ^{13}C NMR solid-state spectra of CNC1 and CNC2. In both spectra, the ^{13}C NMR signals of cellulose appear at 98–110 ppm for C1 (105.3 ppm) and at 80–90 ppm for C4, where the peak near 90 ppm (89.1 ppm) is associated with the highly ordered cellulose chain in the crystallite core (Ic), while the peak farther away (84.2 ppm) corresponds to the C4 of

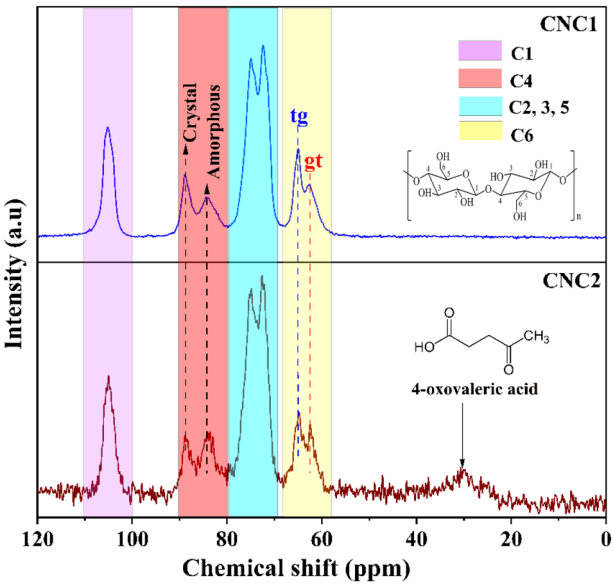

Fig. 11 ^{13}C NMR spectra of CNC1 and CNC2.

disordered cellulose (Ia).[114] This region has been widely studied because it provides important information about cellulose I (Iβ and Iα), para-crystalline and accessible fibril surface (for solvent),[115] or inaccessible fibril surface (interior) and C4 in hemicellulose if this polysaccharide is present in the sample.[116] The results indicate that neither spectrum shows a peak around 173.4 ppm (Fig. S5), which is associated with carbonyl groups (esters and carboxylic acids) in hemicellulose.[117] Therefore, the double peak at 80–90 ppm is a characteristic signal for C4 in cellulose.

Fig. 11 shows that the relative intensity ratio between the two peaks of C4 (Ia/Ic) in CNC2 is higher than in CNC1. This finding agrees with the Raman spectrum mentioned above. Signals assigned to C2, C3, and C5 in the lactone ring were observed at 72.6 ppm and 75.2 ppm, respectively, while C6 appears around 67–60 ppm. Notably, C6 has significant freedom to rotate (mobility) among tg, gt, and gg conformers unless it is restricted by stable hydrogen bonding.[118,119] For example, in cellulose I, C6 is fixed in the tg position, whereas cellulose II typically shows a gt conformation. Compared to CNC1, the NMR spectrum of CNC2 shows a decrease in the peak intensity at 64.9 ppm, which corresponds to the C6 carbon of the tg conformation, while the peak at 62.5 ppm, representing the C6 carbon in conformation II, increases. Additionally, the spectrum of CNC2 shows a broad signal at 30 ppm, attributed to levulinic (or 4-oxovaleric) acid ($C_5H_8O_3$). Levulinic acid and glucose are two main degradation products of cellulose in an acid solution. Levulinic acid can be used to synthesize fuel additives, catalysts, solvents, and herbicides.[120]

4. Conclusions

Rice straw (RS), with its high cellulose content, is a promising alternative to wood for cellulose production. Bleaching is essential for removing hemicelluloses and lignin and overcoming RS recalcitrance. This study examines the effects of alkaline hydrogen peroxide (AHP) and hydrogen peroxide-acetic acid (HPAA) bleaching on the structure, morphology, and thermal stability of cellulose nanocrystals (CNC) derived from RS. AHP bleaching does not fully disrupt the conjugated double bonds in lignin, but subsequent H_2SO_4 hydrolysis removes the remaining lignin, yielding CNC1 with a cellulose I structure, high thermal stability, and rod-like morphology. In contrast, HPAA bleaching effectively removes lignin and introduces carbonyl groups on the cellulose surface, increasing fiber flexibility and facilitating sulfuric acid penetration. This process disrupts hydrogen-bond networks, leading to dissolution, regeneration, and acid hydrolysis, and converts most cellulose into cellulose II. CNC2 exhibits a spherical morphology and lower thermal stability than CNC1, due to surface sulfate groups. The results also show that the K–K method effectively evaluates hemicellulose and lignin removal during chemical processing. Overall, hydrogen peroxide-acetic acid bleaching is an efficient and environmentally friendly alternative for whitening cellulose from agricultural waste.

Author contributions

An Nang Vu: conceptualization, investigation, writing – review & editing. Ngoc-Uyen T. Nguyen: investigation, writing – original draft. Truc-Lam T. Nguyen: formal analysis. Van-Anh T. Nguyen: resources.

Conflicts of interest

There are no conflicts to declare.

Data availability

Data will be made available on request.

Supplementary information (SI) is available. See DOI: https://doi.org/10.1039/d6ra00911e.

Acknowledgements

This research is funded by University of Science, VNU-HCM under grant number T2024-63. The authors are grateful for this financial support.

References

1 T. Li, C. Chen, A. H. Brozena, J. Y. Zhu, L. Xu, C. Driemeier, J. Dai, O. J. Rojas, A. Isogai, L. Wågberg and L. Hu, *Nature*, 2021, **590**, 47–56.
2 H. K. Sharma, C. Xu and W. Qin, *Waste Biomass Valorization*, 2019, **10**, 235–251.
3 Y. Habibi, L. A. Lucia and O. J. Rojas, *Chem. Rev.*, 2010, **110**, 3479–3500.
4 M. Rajinipriya, M. Nagalakshmaiah, M. Robert and S. Elkoun, *ACS Sustainable Chem. Eng.*, 2018, **6**, 2807–2828.

5 N. Y. Abu-Thabit, A. A. Judeh, A. S. Hakeem, A. Ul-Hamid, Y. Umar and A. Ahmad, *Int. J. Biol. Macromol.*, 2020, **155**, 730–739.
6 N. Španić, V. Jambreković and M. Klarić, *Cellul. Chem. Technol.*, 2018, **52**, 163–169.
7 R. Liu, H. Yu and Y. Huang, *Cellulose*, 2005, **12**, 25–34.
8 P. V. Krasteva, J. Bernal-Bayard, L. Travier, F. A. Martin, P.-A. Kaminski, G. Karimova, R. Fronzes and J.-M. Ghigo, *Nat. Commun.*, 2017, **8**, 2065.
9 L. Van Hai, H. N. Son and Y. B. Seo, *Cellulose*, 2015, **22**, 1789–1798.
10 Y. Nishiyama, J. Sugiyama, H. Chanzy and P. Langan, *J. Am. Chem. Soc.*, 2003, **125**, 14300–14306.
11 Y. Nishiyama, P. Langan and H. Chanzy, *J. Am. Chem. Soc.*, 2002, **124**, 9074–9082.
12 K. Gardner and J. Blackwell, *Biopolymers*, 1974, **13**, 1975–2001.
13 P. Langan, Y. Nishiyama and H. Chanzy, *J. Am. Chem. Soc.*, 1999, **121**, 9940–9946.
14 A. Šturcová, I. His, T. J. Wess, G. Cameron and M. C. Jarvis, *Biomacromolecules*, 2003, **4**, 1589–1595.
15 A. N. Vu, L. H. Nguyen, H.-C. V. Tran, K. Yoshimura, T. D. Tran, H. Van Le and N.-U. T. Nguyen, *RSC Adv.*, 2024, **14**, 2048–2060.
16 M. Martínez-Sanz, A. A. Vicente, N. Gontard, A. Lopez-Rubio and J. M. Lagaron, *Cellulose*, 2015, **22**, 535–551.
17 B. M. R. Guimarães, M. V. Scatolino, M. A. Martins, S. R. Ferreira, L. M. Mendes, J. T. Lima, M. G. Junior and G. H. D. Tonoli, *Environ. Sci. Pollut. Res.*, 2022, **29**, 8665–8683.
18 A. Ganesan and J. Rengarajan, *Iran. Polym. J.*, 2024, **33**, 1157–1170.
19 J. Mantovan, G. A. G. Giraldo, B. M. Marim, P. S. Garcia, A. M. Baron and S. Mali, *Biomass Convers. Biorefin.*, 2023, **13**, 1633–1644.
20 F. Debiagi, P. C. S. Faria-Tischer and S. Mali, *Waste Biomass Valorization*, 2021, **12**, 1051–1060.
21 L. Bhatia, H. Jha, T. Sarkar and P. K. Sarangi, *Int. J. Environ. Res. Public Health*, 2023, **20**, 2318.
22 G. Allegretti, M. A. Montoya, L. A. S. Bertussi and E. Talamini, *Renewable Sustainable Energy Rev.*, 2022, **168**, 112860.
23 P. Lu and Y.-L. Hsieh, *Carbohydr. Polym.*, 2012, **87**, 564–573.
24 G. Fan, M. Wang, C. Liao, T. Fang, J. Li and R. Zhou, *Carbohydr. Polym.*, 2013, **94**, 71–76.
25 A. Morone, G. Sharma, A. Sharma, T. Chakrabarti and R. A. Pandey, *Renewable Energy*, 2018, **120**, 88–97.
26 R. Mohd Zainol, R. A. C. Rose, J. Mapjabil and M. Marzuki, *Int. J. Asian Soc. Sci*, 2019, **9**, 295–303.
27 A. Zoghlami and G. Paës, *Front. Chem.*, 2019, **7**, 874.
28 J. Baruah, B. K. Nath, R. Sharma, S. Kumar, R. C. Deka, D. C. Baruah and E. Kalita, *Front. Energy Res.*, 2018, **6**, 141.
29 J.-H. Choi, S.-Y. Park, J.-H. Kim, S.-M. Cho, S.-K. Jang, C. Hong and I.-G. Choi, *Bioresour. Technol.*, 2019, **291**, 121913.
30 N. E. Fitriana, A. Suwanto, T. H. Jatmiko, S. Mursiti and D. J. Prasetyo, *IOP Conf. Ser.: Earth Environ. Sci.*, 2020, **462**, 012053.
31 R. P. Wool, in *Bio-Based Polymers and Composites*, ed. R. P. Wool and X. S. Sun, Academic Press, Burlington, 2005, pp. 551–598, DOI: 10.1016/B978-012763952-9/50017-4.
32 I. W. Arnata, F. Fahma, N. Richana and T. C. Sunarti, *Orient. J. Chem.*, 2019, **35**, 8–19.
33 Y. Song, S. G. Wi, H. M. Kim and H.-J. Bae, *Bioresour. Technol.*, 2016, **214**, 30–36.
34 P.-O. Westin, X. Yang, A. Svedberg, H. Grundberg and L. A. Berglund, *Cellulose*, 2021, **28**, 1873–1880.
35 S. Mayta, R. G. Huamani-Palomino, B. M. Córdova, E. Rivera and M. Quintana, *Biomass Convers. Biorefin.*, 2025, **15**, 24571–24583.
36 J. S. Kim, Y. Y. Lee and T. H. Kim, *Bioresour. Technol.*, 2016, **199**, 42–48.
37 V. Sharma, M.-L. Tsai, C.-W. Chen, P.-P. Sun, A. K. Patel, R. R. Singhania, P. Nargotra and C.-D. Dong, *Bioresour. Technol.*, 2022, **360**, 127631.
38 K. Zhang, Z. Pei and D. Wang, *Bioresour. Technol.*, 2016, **199**, 21–33.
39 P. Wen, T. Zhang, J. Wang, Z. Lian and J. Zhang, *Biotechnol. Biofuels*, 2019, **12**, 87.
40 T. R. Mota, D. M. Oliveira, G. R. Morais, R. Marchiosi, M. S. Buckeridge, O. Ferrarese-Filho and W. D. dos Santos, *Ind. Crops Prod.*, 2019, **140**, 111657.
41 V. Nang An, H. T. Chi Nhan, T. D. Tap, T. T. T. Van, P. Van Viet and L. Van Hieu, *J. Polym. Environ.*, 2020, **28**, 1465–1474.
42 R. M. Dos Santos, W. P. F. Neto, H. A. Silvério, D. F. Martins, N. O. Dantas and D. Pasquini, *Ind. Crops Prod.*, 2013, **50**, 707–714.
43 C. A. Schneider, W. S. Rasband and K. W. Eliceiri, *Nat. Methods*, 2012, **9**, 671–675.
44 S.-C. Shi and G.-T. Liu, *Cellulose*, 2021, **28**, 6147–6158.
45 W. Ying, F. Sun, X. Li and J. Zhang, *Ind. Crops Prod.*, 2023, **197**, 116588.
46 E. S. Abdel-Halim and S. S. Al-Deyab, *Carbohydr. Polym.*, 2011, **86**, 988–994.
47 H. E. Emam, H. B. Ahmed, E. Gomaa, M. H. Helal and R. M. Abdelhameed, *Cellulose*, 2020, **27**, 7139–7155.
48 M. Abdin, M. Mabrouk, L. El-Sebaiy, M. Eissa, M. El-Bana, M. A. Salama, A. E. El-Beltagy and M. A. Naeem, *Int. J. Biol. Macromol.*, 2023, **240**, 124474.
49 R. M. Abdelhameed, H. Abdel-Gawad and H. E. Emam, *J. Environ. Chem. Eng.*, 2021, **9**, 105121.
50 M. Hasanin, R. M. Abdelhameed, S. Dacrory, H. Abou-Yousef and S. Kamel, *Mater. Sci. Eng., B*, 2021, **270**, 115231.
51 H. Ren, Z. Xu, C. Du, Z. Ling, W. Yang, L. Pan, Y. Tian, W. Fan and Y. Zheng, *Int. J. Biol. Macromol.*, 2023, **242**, 124938.
52 D. Kapdi, N. Bhavsar and D. Rudakiya, *Bioresour. Technol. Rep.*, 2024, **25**, 101732.
53 G. Toscano, V. Maceratesi, E. Leoni, P. Stipa, E. Laudadio and S. Sabbatini, *Fuel*, 2022, **313**, 123017.

54 Y. Zhou, Y. Hu, Z. Tan and T. Zhou, *J. Cleaner Prod.*, 2024, **439**, 140839.
55 H. M. Zendrato, N. Masruchin, S. Nikmatin and N. J. Wistara, *J. Ind. Eng. Chem.*, 2024, **131**, 376–387.
56 V. A. Barbash, O. V. Yashchenko, O. S. Yakymenko and V. D. Myshak, *Appl. Nanosci.*, 2023, **13**, 7455–7468.
57 T. A. Do, L. L. Nguyen, T. K. Nguyen Thi and V. Q., *Polymers*, 2025, **17**(15), 2124.
58 Y. Habibi, H. Chanzy and M. R. Vignon, *Cellulose*, 2006, **13**, 679–687.
59 P. K. Mishra, A. Ahuja, B. K. Mahur and V. K. Rastogi, *Express Polym. Lett.*, 2023, **17**, 196–210.
60 I. Kusmono, R. F. Listyanda, M. W. Wildan and M. N. Ilman, *Heliyon*, 2020, **6**, e05486.
61 E. Gümüskaya, M. Usta and H. Kirci, *Polym. Degrad. Stab.*, 2003, **81**, 559–564.
62 F. Khili, J. Borges, P. L. Almeida, R. Boukherroub and A. D. Omrani, *Waste Biomass Valorization*, 2018, 1–15.
63 A. Nang Vu, L. Hoang Nguyen, K. Yoshimura, T. Duy Tran and H. Van Le, *Arabian J. Chem.*, 2024, **17**, 105841.
64 A. D. French and M. Santiago Cintrón, *Cellulose*, 2013, **20**, 583–588.
65 S. Park, J. O. Baker, M. E. Himmel, P. A. Parilla and D. K. Johnson, *Biotechnol. Biofuels*, 2010, **3**, 1–10.
66 L. Xing, J. Gu, W. Zhang, D. Tu and C. Hu, *Carbohydr. Polym.*, 2018, **192**, 184–192.
67 X. Zhang, C. Fang, Y. Cheng, M. Li and J. Liu, *Int. J. Biol. Macromol.*, 2024, **268**, 131984.
68 S. Collazo-Bigliardi, R. Ortega-Toro and A. Chiralt Boix, *Carbohydr. Polym.*, 2018, **191**, 205–215.
69 H. Doh, M. H. Lee and W. S. Whiteside, *Food Hydrocolloids*, 2020, **102**, 105542.
70 M. M. de Souza Lima and R. Borsali, *Macromol. Rapid Commun.*, 2004, **25**, 771–787.
71 A. F. Tarchoun, D. Trache and T. M. Klapötke, *Int. J. Biol. Macromol.*, 2019, **138**, 837–845.
72 J. Baruah, R. C. Deka and E. Kalita, *Int. J. Biol. Macromol.*, 2020, **154**, 672–682.
73 Z. Zhou, D. Ouyang, D. Liu and X. Zhao, *Bioresour. Technol.*, 2023, **367**, 128208.
74 R. Ma, U. Sanyal, M. V. Olarte, H. M. Job, M. S. Swita, S. B. Jones, P. A. Meyer, S. D. Burton, J. R. Cort, M. E. Bowden, X. Chen, M. P. Wolcott and X. Zhang, *Green Chem.*, 2021, **23**, 8468–8479.
75 X. Shao, J. Wang, Z. Liu, N. Hu, M. Liu and Y. Xu, *Ind. Crops Prod.*, 2020, **151**, 112457.
76 A. F. Owolabi, M. K. M. Haafiz, M. S. Hossain, M. H. Hussin and M. R. N. Fazita, *Int. J. Biol. Macromol.*, 2017, **95**, 1228–1234.
77 Y. Liu, A. Liu, S. A. Ibrahim, H. Yang and W. Huang, *Int. J. Biol. Macromol.*, 2018, **111**, 717–721.
78 S. Ventura-Cruz, N. Flores-Alamo and A. Tecante, *Int. J. Biol. Macromol.*, 2020, **155**, 324–329.
79 A. Merci, A. Urbano, M. V. E. Grossmann, C. A. Tischer and S. Mali, *Food Res. Int.*, 2015, **73**, 38–43.
80 L. K. Kian, N. Saba, M. Jawaid and H. Fouad, *Int. J. Biol. Macromol.*, 2020, **156**, 347–353.
81 L. K. Kian, M. Jawaid, H. Ariffin and O. Y. Alothman, *Int. J. Biol. Macromol.*, 2017, **103**, 931–940.
82 B. Debnath, P. Duarah and M. K. Purkait, *Int. J. Biol. Macromol.*, 2023, **244**, 125354.
83 Y. Wu, C. Luo, L. Li, Y. Jiang, J. Yu, T. Wang, J. Lu, X. Cao, W. Ke and S. Li, *Int. J. Biol. Macromol.*, 2024, **267**, 131444.
84 J. Gong, J. Li, J. Xu, Z. Xiang and L. Mo, *RSC Adv.*, 2017, **7**, 33486–33493.
85 M. Cheng, Z. Qin, Y. Liu, Y. Qin, T. Li, L. Chen and M. Zhu, *J. Mater. Chem. A*, 2014, **2**, 251–258.
86 B. Liu, Y. Li, Y. Yuan, B. Zheng, C. Liu, L. Zhou and J. Zhang, *Int. J. Biol. Macromol.*, 2023, **243**, 125119.
87 M. Cheng, Z. Qin, Y. Chen, J. Liu and Z. Ren, *Cellulose*, 2017, **24**, 3243–3254.
88 Y. Ding, O. A. Ezekoye, S. Lu and C. Wang, *Energy Convers. Manage.*, 2016, **120**, 370–377.
89 K.-Y. Li, X. Huang, C. Fleischmann, G. Rein and J. Ji, *Energy Fuels*, 2014, **28**, 6130–6139.
90 H. Cai, J. Liu, W. Xie, J. Kuo, M. Buyukada and F. Evrendilek, *Energy Convers. Manage.*, 2019, **184**, 436–447.
91 L. Lin, Y. E, Q. Sun, Y. Chen, W. Dai, Z. Bao, W. Niu and J. Meng, *Molecules*, 2025, **30**, 10.
92 H. Yang, R. Yan, H. Chen, C. Zheng, D. H. Lee and D. T. Liang, *Energy Fuels*, 2006, **20**, 388–393.
93 A. J. Tsamba, W. Yang and W. Blasiak, *Fuel Process. Technol.*, 2006, **87**, 523–530.
94 N. Lin and A. Dufresne, *Nanoscale*, 2014, **6**, 5384–5393.
95 M. Roman and W. T. Winter, *Biomacromolecules*, 2004, **5**, 1671–1677.
96 M. A. Henrique, W. P. Flauzino Neto, H. A. Silvério, D. F. Martins, L. V. A. Gurgel, H. d. S. Barud, L. C. d. Morais and D. Pasquini, *Ind. Crops Prod.*, 2015, **76**, 128–140.
97 U. P. Agarwal, S. A. Ralph, C. Baez and R. S. Reiner, *Cellulose*, 2021, **28**, 9069–9079.
98 Q. Li and S. Renneckar, *Biomacromolecules*, 2011, **12**, 650–659.
99 R. Panyathip, M. Witthayapak, P. Thuephloi, J. Sukunta, P. Thipchai, S. Thanakkasaranee, K. Jantanasakulwong and P. Rachtanapun, *Ind. Crops Prod.*, 2025, **228**, 120887.
100 K. Schenzel and S. Fischer, *Cellulose*, 2001, **8**, 49–57.
101 J. H. Wiley and R. H. Atalla, *Carbohydr. Res.*, 1987, **160**, 113–129.
102 M. Makarem, C. M. Lee, K. Kafle, S. Huang, I. Chae, H. Yang, J. D. Kubicki and S. H. Kim, *Cellulose*, 2019, **26**, 35–79.
103 H. G. Edwards, N. F. Nikhassan, D. W. Farwell, P. Garside and P. Wyeth, *J. Raman Spectrosc.*, 2006, **37**, 1193–1200.
104 K. Kavkler and A. Demšar, *Spectrochim. Acta, Part A*, 2011, **78**, 740–746.
105 K. Zhang, E. Brendler and S. Fischer, *Cellulose*, 2010, **17**, 427–435.
106 U. P. Agarwal, Raman spectroscopy in the analysis of cellulose nanomaterials, in *Nanocelluloses: their preparation, properties, and applications, ACS symposium series*, American Chemical Society, Washington, DC, 2017, ch. 4, pp. 75–91.

107 M. Adsul, S. K. Soni, S. K. Bhargava and V. Bansal, *Biomacromolecules*, 2012, **13**, 2890–2895.
108 C.-F. Yan, H.-Y. Yu and J.-M. Yao, *Cellulose*, 2015, **22**, 3773–3788.
109 X. Hao, W. Shen, Z. Chen, J. Zhu, L. Feng, Z. Wu, P. Wang, X. Zeng and T. Wu, *Carbohydr. Polym.*, 2015, **123**, 297–304.
110 Y. Ahn, Y. Song and H. Kim, *ACS Macro Lett.*, 2017, **6**, 762–767.
111 Y.-L. Hsieh, *J. Mater. Sci.*, 2013, **48**, 7837–7846.
112 G. Yan, X. Zhang, M. Li, X. Zhao, X. Zeng, Y. Sun, X. Tang, T. Lei and L. Lin, *ACS Sustainable Chem. Eng.*, 2019, **7**, 2151–2159.
113 O. Tzhayik, I. N. Pulidindi and A. Gedanken, *Ind. Eng. Chem. Res.*, 2014, **53**, 13871–13880.
114 W. P. Flauzino Neto, J.-L. Putaux, M. Mariano, Y. Ogawa, H. Otaguro, D. Pasquini and A. Dufresne, *RSC Adv.*, 2016, **6**, 76017–76027.
115 K. Wickholm, P. T. Larsson and T. Iversen, *Carbohydr. Res.*, 1998, **312**, 123–129.
116 X.-F. Sun, R.-C. Sun, Y. Su and J.-X. Sun, *J. Agric. Food Chem.*, 2004, **52**, 839–847.
117 A. Golchin, J. Oades, J. Skjemstad and P. Clarke, *Aust. J. Soil Res.*, 1994, **32**, 285–309.
118 A. N. Fernandes, L. H. Thomas, C. M. Altaner, P. Callow, V. T. Forsyth, D. C. Apperley, C. J. Kennedy and M. C. Jarvis, *Proc. Natl. Acad. Sci. U. S. A.*, 2011, **108**, E1195–E1203.
119 C. M. Lee, A. Mittal, A. L. Barnette, K. Kafle, Y. B. Park, H. Shin, D. K. Johnson, S. Park and S. H. Kim, *Cellulose*, 2013, **20**, 991–1000.
120 G. Butera, C. De Pasquale, A. Maccotta, G. Alonzo and P. Conte, *Cellulose*, 2011, **18**, 1499–1507.